MATERIALS SCIENCE

Porous liquid metal–elastomer composites with high leakage resistance and antimicrobial property for skin-interfaced bioelectronics

Yadong Xu[1]†, Yajuan Su[2]†, Xianchen Xu[3]†, Brian Arends[3], Ganggang Zhao[3], Daniel N. Ackerman[4], Henry Huang[5], St. Patrick Reid[6], Joshua L. Santarpia[6], Chansong Kim[7], Zehua Chen[1], Sana Mahmoud[8], Yun Ling[3], Alexander Brown[9], Qian Chen[7], Guoliang Huang[3]*, Jingwei Xie[2]*, Zheng Yan[1,3]*

Liquid metal–elastomer composite is a promising soft conductor for skin-interfaced bioelectronics, soft robots, and others due to its large stretchability, ultrasoftness, high electrical conductivity, and mechanical-electrical decoupling. However, it often suffers from deformation-induced leakage, which can smear skin, deteriorate device performance, and cause circuit shorting. Besides, antimicrobial property is desirable in soft conductors to minimize microbial infections. Here, we report phase separation–based synthesis of porous liquid metal–elastomer composites with high leakage resistance and antimicrobial property, together with large stretchability, tissue-like compliance, high and stable electrical conductivity over deformation, high breathability, and magnetic resonance imaging compatibility. The porous structures can minimize leakage through damping effects and lower percolation thresholds to reduce liquid metal usage. In addition, epsilon polylysine is loaded into elastic matrices during phase separation to provide antimicrobial property. The enabled skin-interfaced bioelectronics can monitor cardiac electrical and mechanical activities and offer electrical stimulations in a mechanically imperceptible and electrically stable manner even during motions.

INTRODUCTION

Elastic soft conductive materials that exhibit tissue-like compliance and high stretchability are critical for next-generation skin-interfaced bioelectronics because they need to intimately touch soft biological tissues for long periods of time and require electronic materials to function stably and reliably under dynamic deformations. During the past decade, substantial progresses have been achieved to endow conductive materials with high stretchability, mainly including (i) enabling nonstretchable inorganic materials stretchable via structural designs (e.g., serpentine, wavy, island-bridge, and kirigami) and (ii) developing intrinsically stretchable materials (e.g., organic conductors, elastomer composites, and hydrogels) (*1*–*8*). While these methods offer remarkable levels of freedom to make stretchable conductors, they usually face one or more limitations. For example, structural designs do not alter the material's microscopic rigidity and therefore leads to a distinct mismatch in elastic moduli of rigid inorganic materials and soft biological tissues. Organic conductors often suffer from relatively high elastic moduli and low electrical conductivity. In addition, hydrogels usually face challenges of poor electrical conductivity and limited long-term stability due to dehydration.

Among these strategies, embedding conductive fillers into elastomers is promising because it integrates the complementary advantages of the fillers' high electrical conductivity with the elastomers' superelasticity, stretchability, and tissue-like compliance (*9*–*11*). As compared to rigid inorganic fillers [e.g., silver nanowires (AgNWs) and silver (Ag) flakes], liquid metal, particularly eutectic gallium-indium (EGaIn; melting point: ~15.7°C) nano/microparticles composed of EGaIn cores and gallium oxide shells (Ga_2O_3; ~3 nm thick), has raised increasing interests due to its high metallic electrical conductivity (~3.4×10^6 S/m), liquid-like fluidity, negligible vapor pressure (~10^{-44} atm), and nontoxicity (*12*). Recently, EGaIn-embedded elastomer composites with large stretchability, high electrical conductivity, and small conductance variations over deformation have been developed (*13*–*15*). In addition, breathable EGaIn-elastomer composites were achieved by directly coating bulk EGaIn on fibrous mat surfaces (*16*). However, liquid metal–embedded elastomer composites usually suffer from undesired leaking upon deformations (*15*), which not only smears skin but also deteriorates device performance and induces electrical shorting. For instance, the resistance of the liquid metal fiber mat increases ~50% when it is rubbed against human skin (*16*). Encapsulation can minimize leakage and improve durability but will complicate fabrication process and prevent applications where conductive materials need to directly interface with human skin (e.g., cutaneous bioelectronic sensing and stimulating).

In addition, antimicrobial property is desirable for skin-interfaced bioelectronics because their long-term home-based applications can inevitably increase risks of foreign pathogenic microbial

[1]Department of Biomedical, Biological and Chemical Engineering, University of Missouri, Columbia, MO 65211, USA. [2]Department of Surgery-Transplant and Mary and Dick Holland Regenerative Medicine Program, University of Nebraska Medical Center, Omaha, NE 68198, USA. [3]Department of Mechanical & Aerospace Engineering, University of Missouri, Columbia, MO 65211, USA. [4]National Strategic Research Institute, Omaha, NE 68106, USA. [5]School of Aeronautics and Astronautics, Purdue University, West Lafayette, IN 47907, USA. [6]Department of Pathology and Microbiology, University of Nebraska Medical Center, Omaha, NE 68130, USA. [7]Department of Materials Science and Engineering, University of Illinois at Urbana-Champaign, Urbana, IL 61801, USA. [8]Department of Computer Science, North Carolina State University, Raleigh, NC 27695, USA. [9]Cognitive Neuroscience Systems Core, University of Missouri, Columbia, MO 65211, USA.
*Corresponding author. Email: yanzheng@missouri.edu (Z.Y.); jingwei.xie@unmc.edu (J.X.); huangg@missouri.ed (G.H.)
†These authors contributed equally to this work.

infections and disturb skin internal microbial balances (*17*). This demand is further enhanced because of recent frequent occurrences of various infectious diseases [e.g., avian influenza and coronavirus disease 2019 (COVID-19)]. Conductors based on Ag and copper (Cu) nanostructures indicate promising antibacterial property but suffer from some limitations, e.g., high rigidity, easy oxidation, large conductance change upon deformation, and potential adverse health effects of released metal ions (*18*–*20*). In addition, the research of developing antimicrobial soft conductors, which can inhibit foreign pathogenic bacterial and virus infections and preserve skin internal microbial symbiosis, is still nascent.

In this work, we report the phase separation–based synthesis of EGaIn-embedded, porous soft conductors incorporated with epsilon polylysine (ε-PL). The major advances include (i) realizing high leakage resistance under various deformations in liquid metal–embedded soft conductors; (ii) achieving outstanding both antibacterial and antiviral capabilities [gram-negative *Pseudomonas aeruginosa* (PA), gram-positive methicillin-resistant *Staphylococcus aureus* (MRSA), and severe acute respiratory syndrome coronavirus 2 (SARS-CoV-2) for this study], which are still rare in existing soft conductive materials; and (iii) reducing liquid metal usage in elastomer composites due to markedly reduced percolation thresholds. In addition, the obtained porous soft conductor also exhibits large stretchability, tissue-like compliance, high and stable electrical conductance over deformation, high breathability, and magnetic resonance imaging (MRI) compatibility. In addition, the combination of these unique attributes is critical to enable long-term, stable, and sustainable on-skin biomedical operation of soft bioelectronics under versatile daily life scenarios. Furthermore, we exploit its application in skin-interfaced bioelectronics and interconnection cables, which can concurrently monitor cardiac electrical [electrocardiograms (ECGs)] and mechanical [impedance cardiograms (ICGs)] activities, offer programmed electrical stimulations, operate stably and reliably under dynamic deformations, and are mechanically imperceptible to users.

RESULTS

Phase separation–enabled synthesis and outstanding leakage resistance

Conventional methods to prepare liquid metal–elastomer composites usually involve mixing liquid metal micro/nanoscale particles with elastomers (fig. S1) and coalescing particles to generate percolation networks via mechanical or freezing sintering (*12*–*15*). As shown in Fig. 1A, stress caused by mechanical loading (e.g., compression or stretching) can rupture oxide shells and squeeze liquid metal out along conductive pathways, resulting in undesired leakage. To address this issue, we develop porous EGaIn composites using phase separation, where porous structures can provide damping effects to minimize mechanical deformation–induced leakage (Fig. 1B). Moreover, ε-PL, a natural broad spectrum antimicrobial peptide that is regarded as safe as a food preservative (*21*–*24*), is loaded into elastomer matrices during phase separation to offer antibacterial and antiviral property. Here, bis(2-ethylhexyl) sulfosuccinate (BEHS) is used to modify ε-PL (Fig. 1C) to improve its solubility in organic solvents. EGaIn particles (Fig. 1D) and polyurethane (PU) are used as conductive fillers and elastomer matrices, respectively. As illustrated in fig. S2, the fabrication process starts with tip sonication of EGaIn in 1-butanol to break bulk liquid metal into micro/nano-sized particles, followed by addition of the BEHS-modified ε-PL and PU solution in tetrahydrofuran (THF). The resulting precursor solution is drop-casted on an aluminum foil and dried in air. The rapid evaporation of volatile THF (boiling point: 66°C) triggers phase separation of 1-butanol (boiling point: 117.7°C) to form nano/microscale droplets (i.e., PU poor phase). Next, complete evaporation of THF and 1-butanol leads to formation of porous EGaIn composites. During phase separation, EGaIn particles self-organize on pore surfaces due to the Pickering effect (i.e., the segregation of colloidal particles to the interface between two fluids to minimize the free energy of the system; Fig. 1E and fig. S3) (*25*) and collapse to form conductive pathways by mechanical sintering. Last, laser cutting of obtained porous EGaIn composites can define arbitrary patterns (fig. S4) for subsequent device fabrication. The electrical conductivity of the porous EGaIn composite can be tailored by adjusting the EGaIn volume fraction (up to ~1.2×10^6 S/m with ~55% EGaIn volume fraction). For the trade-off between the device performance and EGaIn usage, 25% EGaIn volume fraction is used in this work for characterization and device fabrication. The porosity and electrical conductivity are ~57% and ~2.0×10^5 S/m, respectively.

As compared to nonporous liquid–metal composites, conductive EGaIn pathways of porous composites reside in solid (elastomer)–gas (pore) interfaces and experience substantially lower stress upon mechanical loading because of damping effects of porous structures, thus endowing outstanding leakage resistance under deformation (Fig. 1, F to I). This mechanism is theoretically demonstrated through finite element analysis (FEA) simulations (fig. S5). Here, nonporous and porous EGaIn composites with the same electrical conductivity (~2.0×10^5 S/m) were adopted to compare their leakage resistance. Particularly, Fig. 1F shows that compression can cause evident EGaIn leakage on nonporous composites yet indiscernible leakage on porous composites. After wearing nonporous composites for 3 days, smearing effect is observed on human skin (left panel in Fig. 1G). By contrast, invisible smearing occurred after 3 days for porous composites due to negligible EGaIn leakage (right panel in Fig. 1G). Moreover, EGaIn leakage can deteriorate the device performance and induce circuit shorting. The maximum pressure applied by human finger was ~0.2 MPa, whereas the highest value under human foot during walking is ~0.33 MPa (*26*, *27*); we therefore use 0.4 MPa to examine the potential liquid metal leakage. As shown in Fig. 1H and fig. S6, repetitive compression (0.4 MPa for 100 cycles) can cause circuit shorting of two adjacent conductive traces of nonporous composites but have negligible effects on adjacent traces of porous composites. Similarly, Fig. 1I and fig. S7 indicate cyclic stretching (400% strain for 100 cycles) can induce severe leakage on nonporous composites and negligible leakage on porous composites. The leakage from the nonporous composite in Fig. 1I was estimated to be ~0.22 g/cm^3 at the 400% strain. We also experimentally determined the threshold of the porous composite where EGaIn leakage occurs to be ~0.9 MPa under compression, and no EGaIn leakage was observed before the porous composite ruptured at ~550% strain. After collapsing porous structures via dimethylformamide vapor treatment, EGaIn can readily leak from the collapsed composite upon stretching (fig. S8), further indicating the critical role of porous structures in enabling high leakage resistance. In addition, Fig. 1J demonstrates that the "SMBE" light-emitting diode array, interconnected with conductive traces of porous EGaIn composites patterned on

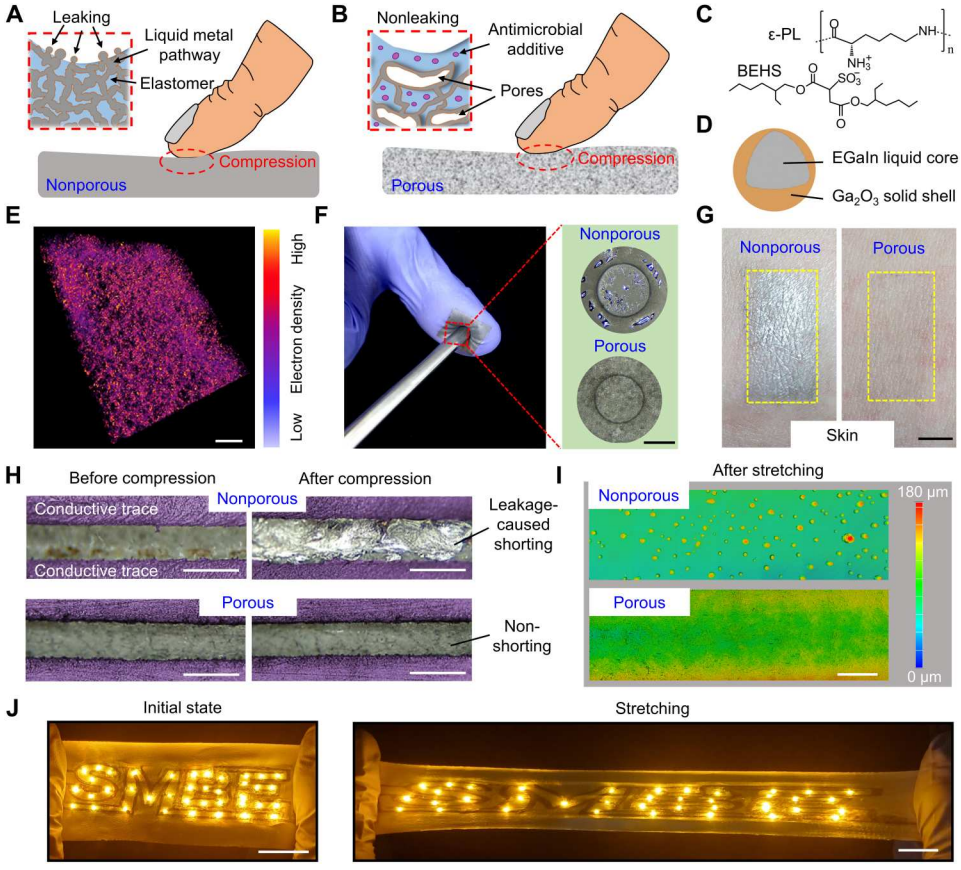

Fig. 1. Leakage-resistant property. Conceptual illustration of conventional nonporous (**A**) and multifunctional porous (**B**) EGaIn composites upon compression. Here, porous structures can provide damping effect to substantially reduce stresses induced on liquid metal conductive pathways (see details in fig. S5), therefore endowing leakage-resistant property. In addition, antimicrobial additive can offer antibacterial and antiviral property. (**C**) Chemical structure of the antimicrobial additive, ε-PL, modified with BEHS for uniform dispersion in solvents. (**D**) Schematic of the EGaIn particle made by tip sonication of bulk EGaIn. (**E**) 3D tomography image of porous composites before sintering, showing EGaIn particle (yellow) distributions in elastomers (pink). Scale bar, 100 μm. (**F**) Photographs of compressing EGaIn composites with a stainless steel rod, demonstrating evident leakage on nonporous composites and indiscernible leakage on porous composites. Scale bar, 500 μm. (**G**) Photographs of human skin after wearing nonporous and porous EGaIn composites for 3 days, showing notable smearing effects induced by nonporous EGaIn composites. Scale bar, 5 mm. (**H**) Photographs of two adjacent conductive traces made of nonporous (top) and porous (bottom) EGaIn composites before and after repetitive compression (0.4 MPa, 100 cycles). Scale bars, 500 μm. (**I**) 3D surface tomography images of porous and nonporous EGaIn composites after cyclic stretching (400%, 100 cycles). Scale bar, 1 mm. (**J**) Photographs of light-emitting diode arrays, interconnected with conductive traces of porous EGaIn composites, at the initial (left) and 200% stretching (right) states. Scale bars, 2 cm.

porous PU, can operate stably and reliably under large stretching (200% strain).

Material characteristics and electromechanical responses

Here, EGaIn particle sizes can be tailored by the tip sonication time (fig. S9). Figure 2A indicates that reducing particle sizes can lower electrical conductivities of the resulting porous EGaIn composites at the same volume fraction (~25% for this study), possibly due to increased amounts of oxide skin layers (i.e., Ga_2O_3). In this work, 2-min sonication is used to make EGaIn particles (~1.26 μm in diameter) for the preparation of EGaIn composites. As compared to nonporous EGaIn composites, phase separation–induced porous structures can markedly lower percolation thresholds of the porous composites. Percolation threshold is a critical point where the electrical conductivity experiences sharp transition as the amount of conductive fillers increases (*14*). Figure 2B indicates that the percolation threshold (~0.07) of the porous composite is considerably lower than that (~0.39) of the nonporous one, due to self-assembly of EGaIn micro/nanoparticles on the pore surfaces instead of uniform distributions in elastomer matrices. Because of the substantially reduced percolation threshold, less amounts of EGaIn are required in the porous composite than that of the nonporous composite to reach the same electrical conductance (fig. S10). For example, the EGaIn usage in porous composites is ~33% of EGaIn used in nonporous composites to reach the electrical conductivity of ~2.0×10^5 S/m, which is sufficient for applications in soft bioelectronic electrodes and conductive interconnects. In addition, a high electrical conductivity of ~1.2×10^6 S/m can be reached when the EGaIn volume fraction is ~55%. Notably, obtained porous EGaIn composites exhibit exceptional electrical uniformity over a large area (fig. S11).

Ideally, soft conductors should retain stable conductance under various deformations (i.e., mechanical-electrical decoupling). This feature is essential to construct bioelectronics and soft robots that

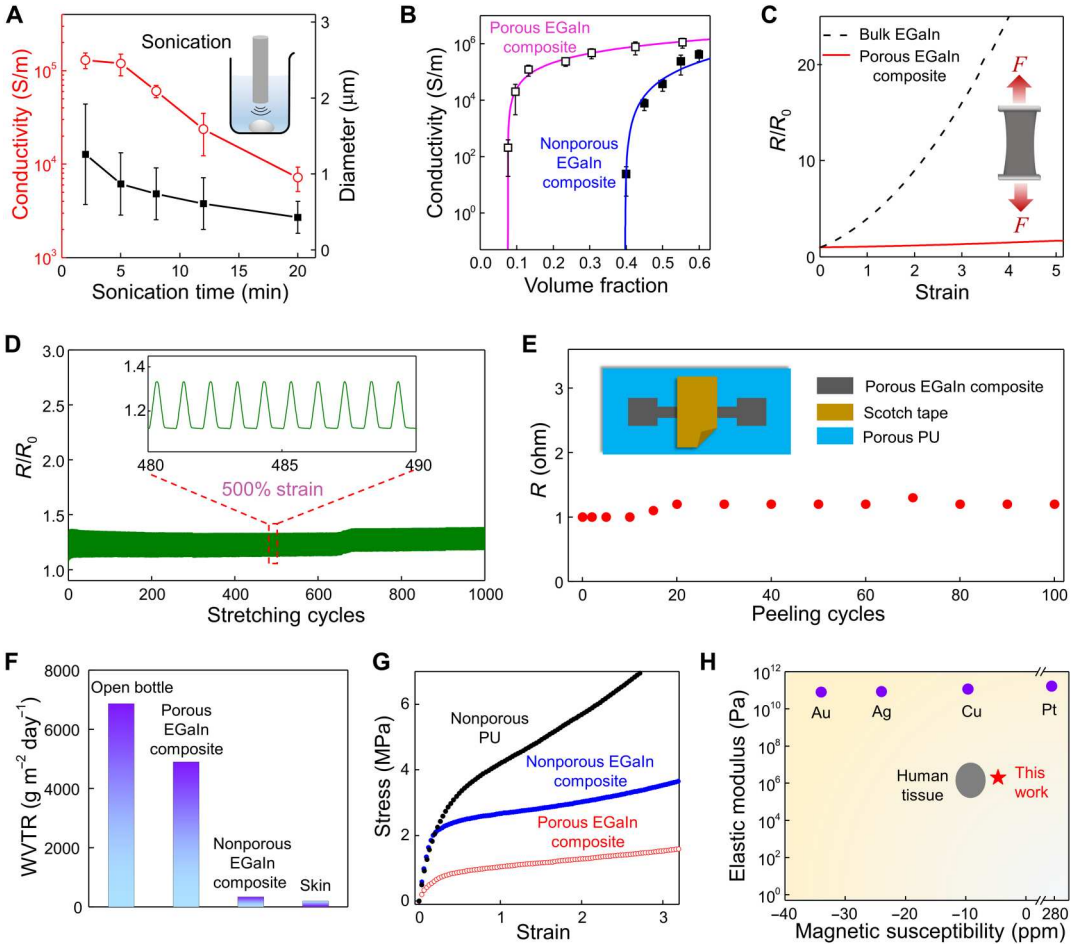

Fig. 2. Material characteristics and electromechanical responses. (**A**) EGaIn particle sizes (black) and electrical conductivities of porous EGaIn composites (red) as a function of the tip sonication time. Inset: Schematic illustration of tip sonication of bulk EGaIn in 1-butanol. (**B**) Electrical conductivities of nonporous and porous EGaIn composites as a function of EGaIn volume fractions. Error bars in (A) and (B) represent SDs of six samples. Pink and blue lines are fitting curves of porous and nonporous EGaIn composites, respectively, using the 3D percolation theory. (**C**) Relative resistance changes (R/R_0) of bulk EGaIn and porous EGaIn composites as a function of uniaxial strains. (**D**) Relative resistance changes of porous EGaIn composites subjected to cyclic stretching (500% maximum strain). (**E**) Resistance changes of porous EGaIn composites under cyclic peeling with scotch tapes. The inset shows the testing setup. (**F**) Water vapor transmission rates (WVTRs) of an open bottle, porous EGaIn composites, nonporous EGaIn composites, and human skin. (**G**) Stress-strain curves of nonporous PU, nonporous EGaIn composites, and porous EGaIn composites, demonstrating the markedly reduced elastic modulus (i.e., ultrasoftness) of the porous EGaIn composite due to its porous structures. (**H**) Comparisons of the elastic modulus and magnetic susceptibility of porous EGaIn composites with some conventional metal conductors and human tissues. ppm, parts per million.

can function stably under various dynamic motions. Figure 2C and fig. S12 indicate that porous EGaIn composites exhibit negligible conductance change upon both uniaxial and biaxial stretching, substantially lower than that of bulk EGaIn predicted by the Pouillet's law (*28*). This unique trait arises from the fluid-like nature of liquid metal, reorientation of tortuous conductive pathways under stretching, and formation of microwrinkles due to the mechanical mismatch of the liquid core and the solid shell (Fig. 1D and fig. S13). In addition, the EGaIn fraction and stretching rate have small effects on electromechanical responses of porous EGaIn composites (fig. S14). Notably, the porous composite exhibits outstanding durability and reliability, as evidenced by ~15% resistance change after cyclic stretching of 500% for 1000 cycles (Fig. 2D). Superior to recently developed breathable liquid metal fiber mats (*16*), the porous EGaIn composites show small resistance changes (~20%) after repetitive peeling for 100 cycles using scotch tapes (Fig. 2E). The outstanding electrical property has also been corroborated and exemplified by the stable and robust ECG recording after up to 100 peeling cycles (fig. S15). Besides, the obtained porous composites also show high electrical stability under ambient conditions, in phosphate-buffered saline (PBS) solutions, by ultraviolet ozone treatment, and after repetitive washing (fig. S16). Given the supercooling effect of liquid metal (*29*) and the high human body temperature, the porous EGaIn composite remains soft and therefore can work in extreme winter scenarios (fig. S17).

Breathability is another required feature for skin-interfaced bioelectronics as it can facilitate skin perspiration and improve their long-term biocompatibility (*30*). The interconnected pores in the porous EGaIn composite can endow high breathability. Figure 2F shows that its water vapor transmission rate (~4900 g m^{-2} day^{-1}) is comparable to that of an open bottle (~6800 g m^{-2} day^{-1}) and notably higher than those of nonporous EGaIn composites (~340

g m^{-2} day^{-1}) and human skin (~200 g m^{-2} day^{-1}) (*31*). It is known that the material's elastic modulus E scales with its density ρ following the equation of $E/E_s \propto (\rho/\rho_s)^n$ (*32*). Here, the power (n) depends on the porous material's nano/microstructures. The porous EGaIn composite's elastic modulus (~1.5 MPa) is ~10 times lower than that of nonporous composites (~16.7 MPa) and comparable to that of human skin (~5 kPa to 140 MPa) (*33*). In addition, it is desirable to develop MRI-compatible soft bioelectronics (*34*, *35*) to collect comprehensive information of human physiological states. Here, the magnetic susceptibility of the porous composite is −3.23 parts per million (ppm) at 300 K and demonstrates negligible dependences on the EGaIn volume fraction (fig. S18), surpassing metal conductors in both the MRI compatibility and tissue-like compliance (Fig. 2H and fig. S19) (*36*).

Antimicrobial (antibacterial and antiviral) property and biocompatibility

Human skin is generally colonized with a diverse milieu of beneficial microorganisms (*37*). Long-lasting, home-based usage of conventional soft bioelectronics in real-life scenarios can disturb skin microbial symbiosis as well as make skin susceptible to foreign pathogenic bacterial and virus infections (Fig. 3, A to D), leading to various skin and/or infectious diseases. Our in vitro and in vivo experiments show that porous EGaIn composites with ε-PL can not only inhibit foreign pathogenic bacteria and virus infections but also retain internal skin bacterial symbiosis (Fig. 3, A to D). Here, two types of skin pathogenic bacteria (i.e., gram-negative PA and gram-positive MRSA) were used for in vitro antibacterial tests, and the bactericidal efficacy was determined by the colony count method (*38*). As indicated in Fig. 3B and fig. S20, the control sample (tissue culture polystyrene) and soft materials without ε-PL, including AgNW-PU composites, show high bacterial viability after 2-hour conditioning. By contrast, both porous PU and porous EGaIn composites with ε-PL indicate extraordinary antibacterial performances, exhibiting more than 95% bactericidal efficacies against PA and MRSA because ε-PL can disrupt bacterial membrane structures (fig. S21) (*21*). Furthermore, on-skin patches (1 cm × 1 cm) made of various soft materials were laminated on human skin (fig. S22) for 5 days to examine their effects on skin microbial symbiosis. Bacterial amounts on skin locations, covered by these patches, were normalized by the bacterial amounts of the closely neighboring bare skins (control). As shown in Fig. 3C, we notice a marked increase of bacterial amounts (~20 times) on skin locations covered by soft patches without ε-PL, whereas bacterial amounts on skin locations covered by porous PU and porous EGaIn composites with ε-PL increased about one time after 5-day wearing, showing their small effects on skin bacterial symbiosis. Quantitative examination of bacterial numbers also showcases notable inhibition of bacterial growth on skin patches with ε-PL (fig. S23). Notably, ε-PL also shows an inhibitory effect in replications of RNA and DNA viruses (e.g., HIV-1 and influenza A viruses) (*23*, *24*). Here, we investigated antiviral efficiencies of porous EGaIn composites with ε-PL against SARS-CoV-2 virus. A volume of 10 μl inoculum containing 3.41×10^7 median tissue culture infectious dose ($TCID_{50}$)/ml of SARS-CoV-2 was dropped onto each sample. Promisingly, ~99.90% of SARS-CoV-2 was inactivated on samples with ε-PL within 30 min (Fig. 3D). This was significantly superior to porous EGaIn composites without ε-PL (61.87%) and steel coupon (53.58%). Notably, the porous EGaIn composite with ε-PL induced a reduction of viable virus titers from 4.53 to 2.98 log($TCID_{50}$/ml), i.e., 97.18% of inactivation even within extremely short contact time (~10 s). To examine biocompatibility of porous composites with ε-PL, we performed cytotoxicity tests using the human myeloid leukemia cell line (U937), human keratinocyte cell line (HaCaT), human dermal fibroblast (HDF) cell line, and mouse embryonic fibroblast (NIH/3T3) cell line. Figure 3E indicates that there are no significant differences ($P > 0.05$) in cell viability among the cells cultured with porous EGaIn composites with ε-PL and on tissue culture polystyrene (control) after 5-day cell culturing. Although mechanical agitation increases the cytotoxicity of liquid metal (*39*), the microscale wrinkles of liquid metals (fig. S13) can efficiently accommodate the mechanical strains and potentially alleviate the leakage of Ga and In ions during dynamic skin deformations. This is further corroborated by cytotoxicity tests with repetitive stretching (50%, 1000 cycles) in artificial perspiration (pH 4.3; Pickering Laboratories; fig. S24), indicating outstanding biocompatibility in a broad range of physiologically relevant pH levels of human perspiration (*40*). Fluorescent live/dead cell staining images (Fig. 3F) show regular live cell (green) morphologies and rare dead cells (red) after 5-day culturing on the porous EGaIn composite and control sample. These results show that porous EGaIn composites with ε-PL show negligible cytotoxicity and outstanding biocompatibility.

Imperceptible, artifact-free skin-interfaced bioelectronics

We investigated skin-interfaced bioelectronic systems, comprising skin-mounted bioelectronic patches with porous EGaIn composite electrodes on porous PU substrates, imperceptible cables of porous EGaIn composites, and mobile data acquisition modules (Fig. 4A and fig. S25). Here, rigid data acquisition modules are clipped onto clothing to avoid direct contact with skin and are connected to skin-mounted bioelectronic patches with superelastic, ultrasoft cables of porous EGaIn composites (Fig. 4B). The enabled wearable system is mechanically imperceptible and comfortable to users (Fig. 4, C to G) and features high-fidelity signal recording even during human motions and in water (Fig. 4, H to K, and figs. S26 to S33). In addition, skin-mounted bioelectronic patches and interconnection cables, based on solution-processed porous composites, are disposable (low-cost and one-time use) to further minimize infection risks, and clothing-clipped data acquisition modules are easily dismantled from the wearable systems for reuse to save cost. Such form of wearable devices should be a valuable addition to existing wearable systems integrated on a single substrate (*41*, *42*).

We first examined the fundamental aspects of mechanical imperception. The skin sensation limit is ~20 kPa, and most mechanoreceptors of sensing stimuli reside in dermis (*41*). Here, we numerically investigated the stress on the skin surface and bottom epidermal layer (80 μm in depth) caused by stretching cables connected to skin-mounted electronic patches (Fig. 4C). The FEA simulations (Fig. 4, D and E) reveal the stresses caused by stretching the porous composite cable and widely used flexible anisotropic conductive film (ACF) cable. To induce the 20-kPa stress on the skin surface, ~0.2 and 46% strains (a factor of ~230) are needed to stretch ACF cables and porous EGaIn composite cables, respectively. Figure 4F provides optical images of stretching porous composite cables and ACF cables from skin at 10% strain. Both simulation and experimental results indicate high imperceptibility of porous EGaIn composite cables as compared to ACF cables. Furthermore,

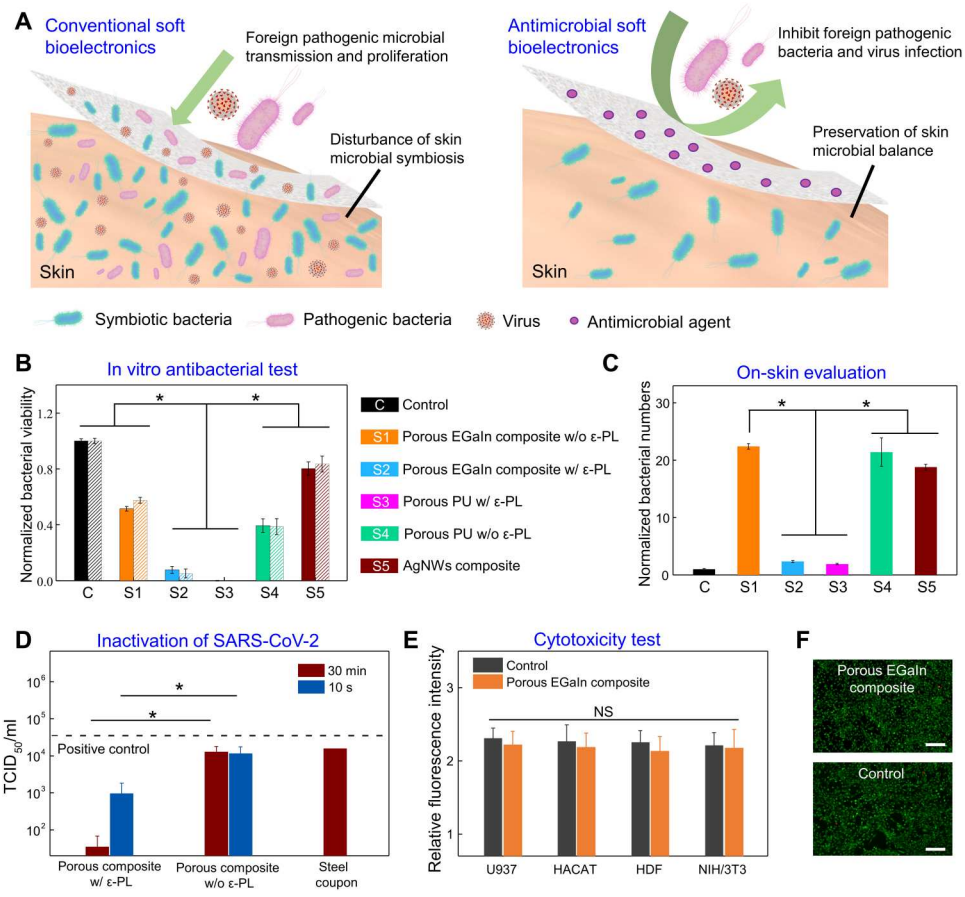

Fig. 3. Antibacterial and antiviral property and biocompatibility. (**A**) Conceptual illustration of conventional (left) and antimicrobial (right) soft bioelectronics for long-lasting, home-based applications. As demonstrated in (B) to (D), the former not only suffers from rapid microbial growth and disturbs skin bacterial symbiosis but also is susceptible to foreign pathogenic bacteria and virus contamination. By contrast, the porous EGaIn composite loaded with ε-PL is capable of inhibiting foreign pathogenic bacteria and virus contamination and preserving skin microbial balance. (**B**) Normalized viabilities of the gram-positive methicillin-resistant *S. aureus* (MRSA) (solid) and gram-negative *P. aeruginosa* (PA) (slash line) conditioned with various materials for 2 hours. (**C**) Normalized bacterial numbers extracted from skin locations covered with various materials for 5 days. (**D**) SARS-CoV-2 titer on porous composites with and without ε-PL after 10-s and 30-min contact and on steel coupon as a comparison. (**E**) Relative fluorescence intensities of the control sample and the porous EGaIn composite with ε-PL after 5-day incubations of U937, HaCaT, HDF, and NIH/3T3 cell lines. (**F**) Fluorescent images of NIH/3T3 cells cultured with the porous EGaIn composite with ε-PL (top) and with the control sample (bottom) for 5 days, showing negligible cell toxicity. Scale bars, 50 μm. Statistical significance and *P* values are determined by one-way analysis of variance (ANOVA) and Tukey's multiple comparison test. $^*P < 0.05$; NS indicates no statistically significant differences.

questionnaires were used to evaluate the discomfort levels of skin-interfaced bioelectronic systems shown in fig. S25, where porous composite cables, ACF cables, and conventional polyvinyl chloride (PVC)–insulated copper wires were respectively used to connect skin-mounted bioelectronic patches with clothing-clipped mobile data acquisition modules. Twenty volunteers were involved and reported discomfort levels with visual analog scales (0 to 10; 0: no discomfort, 10: most discomfort) after wearing the wearable systems for 24 hours. The wearable system interconnected with porous EGaIn composite cables shows a significantly lower discomfort level as compared to those of wearable systems interconnected with ACF cables and PVC-insulated copper wires (Fig. 4G) due to their ultrastretchability and ultrasoftness.

Monitoring heart electrical activity via ECG outside clinical settings plays an indispensable role in diagnosis of heart diseases (*43*, *44*). Concurrent measurement of cardiac mechanical function by ICG can reveal critical information that complements those associated with ECG (*45*–*47*). The wearable system based on porous EGaIn composites can perform high-fidelity ECG and ICG recording even during motions. Particularly, porous EGaIn composite electrodes demonstrate comparable skin-electrode impedances (~70 kilohms) to that of silver/silver chloride (Ag/AgCl) gel electrodes (~65 kilohms) with the same dimension (10 mm × 20 mm) at 100 Hz (fig. S26). Figure 4 (H and I) provides ECG and ICG signals concurrently recorded using porous EGaIn composite electrodes, as illustrated in fig. S27. ECG indicates distinguishable p-wave, QRS complex, and t-wave. The critical characteristic points in ICG are also clearly observable, including B, C, X, and O that represent the opening of the aortic valve, maximum ejection velocity, closing of the aortic valve, and opening of the mitral valve, respectively (*45*). The pre-ejection period (i.e., time elapse between the *Q* point in ECG and *B* point in ICG) represents the period of left ventricular contraction with cardiac valves closed, indicative of heart sympathetic innervation (*47*). Because of the porous

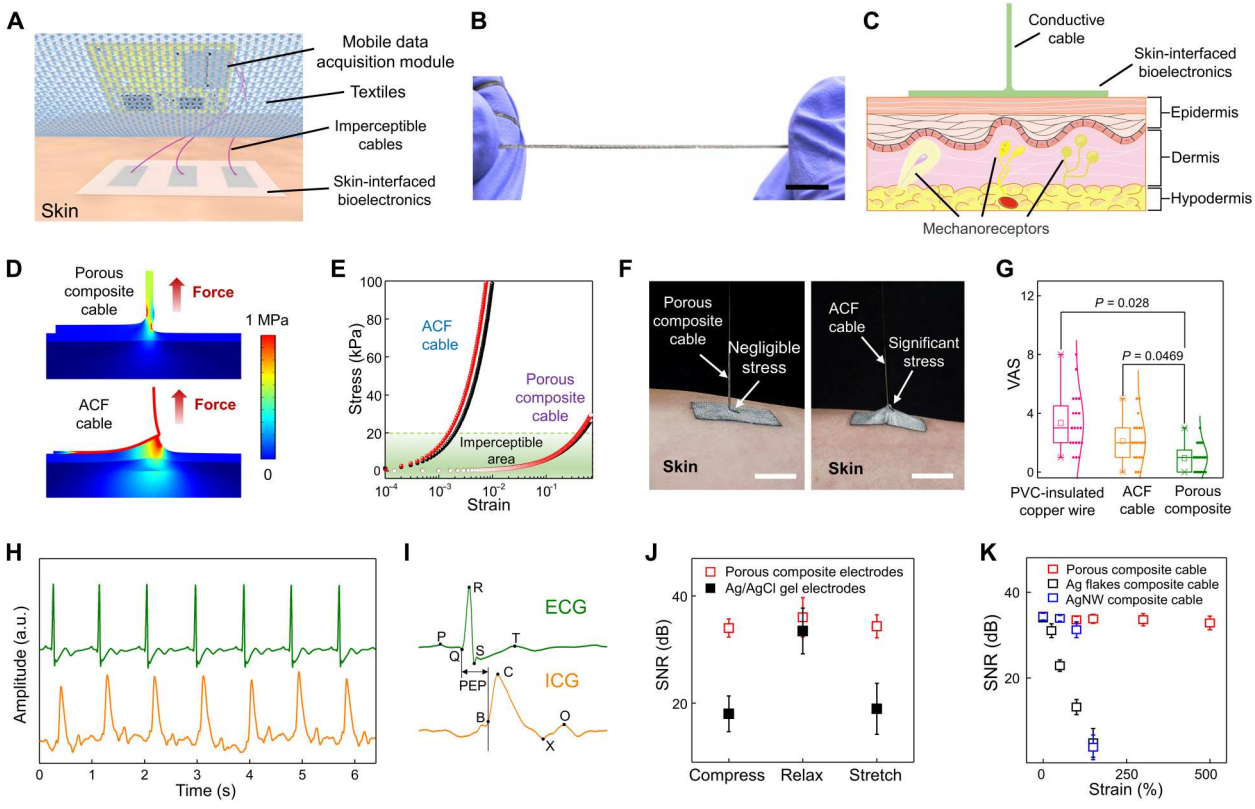

Fig. 4. Imperceptible, artifact-free skin-interfaced bioelectronics. (**A**) Schematic illustration of a skin-interfaced bioelectronic system, comprising skin-mounted bioelectronic patches with porous composite electrodes patterned on porous PU, imperceptible interconnection cables of porous composites, and mobile data acquisition modules. (**B**) Photograph of a porous EGaIn composite cable under high stretching (~500%). Scale bar, 1 cm. (**C**) Schematic of the simplified structure for FEA simulations, together with skin anatomy. (**D**) Simulation results for the von Mises stress distribution when stretching the porous EGaIn composite cable (top, 46% strain) and the ACF cable (bottom, 0.2% strain). (**E**) Simulation results for stresses induced on the skin surface (red) and the bottom epidermis (80 μm in depth; black) as a function of strains applied to the porous EGaIn composite cable and the ACF cable. Imperceptible areas represent the strains at which induced stresses are less than 20 kPa (the perception limit of human skin). (**F**) Photographs of stretching the porous EGaIn composite cable (left) and the ACF cable (right). Here, the initial length and displacement of the porous composite cable and ACF cable are identical. (**G**) Questionnaire results of discomfort levels of 20 volunteers after wearing skin-interfaced bioelectronic systems (fig. S25) for 24 hours, which are interconnected with the porous EGaIn composite cable, ACF cable, and PVC-insulated copper wire. (**H**) Concurrent ECG and ICG recording using skin-interfaced bioelectronics based on porous EGaIn composites. a.u., arbitrary units. (**I**) Magnified ECG and ICG signals in (H). (**J**) SNR of ECG signals recorded with porous composite electrodes and Ag/AgCl electrodes when stretching, relaxing, and compressing the electrodes. (**K**) SNR of ECG signals recorded using porous EGaIn composite electrodes when stretching interconnection cables made of porous EGaIn composites, Ag flakes composites, and AgNWs composites. Error bars in (J) and (K) represent SDs of six samples.

EGaIn composite's large stretchability, ultrasoftness, and stable conductance over strain, the obtained skin-interfaced electrodes and interconnection cables can enable steady biosignal recording with high signal-to-noise ratios (SNRs) under dynamic deformations (Fig. 4, J and K, and figs. S28 and S29), which are superior to conventional Ag/AgCl gel electrodes, as well as interconnection cables made of other soft conductors (e.g., Ag flake–PU composites and AgNW-PU composites). These properties endow reliable and stable signal acquisitions even during motions, as demonstrated by concurrent ECG and ICG signal recording when a human subject rode a stationary bicycle (fig. S30) and ECG monitoring when a human subject rested, walked, and jogged on a treadmill (fig. S31 and movie S1). In addition, porous EGaIn composite electrodes can deliver reliable, programmed electrical stimulations even under deformations (fig. S32). Because of the high hydrophobicity of porous PU (water contact angle, 140°), the enabled skin-interfaced bioelectronics demonstrate excellent waterproofness and can perform high-quality electromyogram (EMG) recording even in water (fig. S33 and movie S2).

DISCUSSION

By introducing a judiciously designed phase separation approach, we have developed EGaIn-based, multifunctional porous soft conductors with high leakage resistance and antimicrobial property, in combination with other desired features such as large stretchability, tissue-like compliance, high and stable electrical conductance over deformation, high breathability, and MRI compatibility. During phase separation, EGaIn particles self-organize on pore surfaces and then form conductive pathways through mechanical sintering, which can not only lower percolation thresholds and reduce EGaIn usage (only requiring ~33% EGaIn used in nonporous composites with the same electrical conductivity at ~2×10^5 S/m) but also minimize deformation-caused liquid metal leakage. Because of the

phase separation–enabled ε-PL incorporation, the obtained porous soft conductor exhibits remarkable antibacterial and antiviral capability against gram-negative PA, gram-positive MRSA, and SARS-CoV-2 virus, which can inactivate 97.18% of SARS-CoV-2 viruses within 10 s. Because of these unique features, it can serve as an ideal soft conductor with built-in multifunctionality to construct both skin-mounted bioelectronic patches and interconnection cables for long-term, home-based biomedical applications. The enabled wearable device can interact with human body in a mechanically imperceptible and comfortable manner and provide high-fidelity, steady biosignal recording and programmed bioelectronic interventions even during motion. This unique porous soft conductor could also find immediate applications to implantable bioelectronics and soft robots.

MATERIALS AND METHODS

Material and device fabrications

The porous EGaIn-PU composite fabrication started with tip sonication (Branson SFX550) of 1 g of bulk EGaIn (75.5% Ga, 24.5% In; Sigma-Aldrich) in 5 ml of 1-butanol at an amplitude of 50% for 2 min. BEHS-modified ε-PL was prepared by following recently reported procedures (*48*) and was added (44 mg) to the EGaIn particle solution. Next, the precursor solution was obtained by mixing the EGaIn particle solution and the PU (Texin RxT85A, Covestro) solution (70 mg/ml in THF) at a volume ratio of 5:4. Drop-casting precursors on aluminum foils and drying under ambient conditions led to the formation of the porous composite film with ~25% EGaIn volume fraction. Subsequently, EGaIn conductive percolation networks were created in composites by mechanical sintering with a stainless steel roller. Here, the EGaIn fraction can be tailored by controlling the amount of added bulk EGaIn. To eliminate the effects of particle sizes, we made EGaIn particles in 1-butanol and redispersed them in PU solutions of THF for the preparation of nonporous EGaIn-PU composites. Ag flake–PU composites (~47% volume fraction) were synthesized by mixing 5.8 g of Ag flakes (10 μm in particle size; Sigma-Aldrich) with 10 ml of PU solutions (70 mg/ml in THF) using a planetary mixer (AR-100, THINKY), followed by drop-casting on aluminum foils and natural drying in air. AgNW-PU composites (~2.5% volume fraction) were prepared using recently reported methods (*49*). Porous composite patterns (fig. S4) were fabricated with a VLS2.30 universal laser system. On-skin electrodes were laminated on porous PU substrates with silicone adhesives (Sil-Poxy, Smooth-On). Skin-mounted devices were attached on skin using Spectra 360 electrode gels (Parker Laboratories). For interconnection cables made of various soft conductive composites, a thin layer of polydimethylsiloxane coating was used for electrical insulation. We have developed a highly conductive PU ink for robust connections. The ink was prepared by dissolving a hydrophilic waterborne PU (HydroMed D3, AdvanSource Biomaterial) adhesive in a mixture of ethanol and deionized water (95:5 by volume) to generate a 10% PU solution (by weight). For 1 g of PU solution, 0.83 g of Ag flakes (10 μm; Sigma-Aldrich) and 2 g of EGaIn were added and mixed using a planetary mixer (Thinky, AR-100) at 2000 rpm.

Characterizations and measurements

Scanning electron microscopy (SEM) images were taken with a FEI Quanta 600 FEG Environmental SEM. The three-dimensional (3D) tomography image in Fig. 1E was constructed using an x-ray microscope (ZEISS Xradia 510 Versa). Images in Fig. 1I were captured by a Leica SP8 spectral confocal microscope. Magnetic susceptibility of porous EGaIn composites was measured by a superconducting quantum interference device (MPMS3, Quantum Design North America, USA). Water vapor transmission rates were determined on the basis of ASTM96 at 35°C. Fluorescence images were taken with a Zeiss Axiovert 40 CFL trinocular inverted fluorescence phase contrast microscope. A 3T Siemens Prisma scanner with a 20-channel head coil was used for MRI scanning. Mechanical properties were characterized using a Mark-10 ESM303 tensile tester. Electrical conductance was measured by a digital source meter (2604B, Keithley Instruments). Skin electrode impedances with identical lateral electrode dimensions (10 mm × 20 mm; center-to-center distance of electrodes, 40 mm) were determined using an LCR meter (IM3523, Hioki). Note that the thickness of the porous EGaIn composite is ~80 μm, much thinner than that of Ag/AgCl electrodes (~1.5 mm in thickness). ECG, EMG, and ICG were recorded using MP160 (BIOPAC Systems). Electrical stimulations were applied using PowerLab T26 (ADInstruments). Mobile wireless data acquisition modules are shown in figs. S34 and S35. A commercial portable ECG monitor (MAX-ECG-MONITOR, Maxim Integrated Inc.) was used as a comparison.

Numerical simulations

Numerical simulations were performed by commercial finite element modeling and analysis software COMSOL Multiphysics. Material properties used in numerical simulations are summarized in table S1.

In vitro cytotoxicity assay

The cytotoxicity tests were carried out following a contact mode protocol using HaCaT, U937, HDF, and NIH/3T3 (*50*). Samples were cut into disks with 1 cm diameter and sterilized with 70% ethanol, followed by rinsing with sterilized PBS. Cells (5×10^4 cells/cm^2) were cultured in 24-well culture plate using Dulbecco's modified Eagle's medium (DMEM) or RPMI 1640 medium (Thermo Fisher Scientific, USA) supplemented with 10% fetal bovine serum (FBS) (Thermo Fisher Scientific, USA). After 6 hours for cell attachment on the culturing plate, the presterilized films were carefully transferred to the wells containing cells, ensuring that it was faced to the cells. The plate containing cells and film was cultured for 5 days, and the culture medium was replaced every 2 days. The viability of the cells contacting with films were determined with alamarBlue assay and LIVE/DEAD assay. alamarBlue assay (Thermo Fisher Scientific, USA) was implemented following the protocol provided by the manufacturer. NIH/3T3 cells were also stained using LIVE/DEAD cell viability kit (Thermo Fisher Scientific, USA) and then examined with an inverted fluorescence microscope (Zeiss, Germany).

Antimicrobial evaluation

The in vitro antimicrobial property of materials was determined following a reported protocol (*38*). Briefly, gram-negative PA E411-17 and gram-positive MRSA USA300 were cultivated in LB medium overnight at 37°C, then recultivated in fresh medium, and grown to OD_{600} (optical density at 600 nm) = 0.5. The two test inoculums were diluted to a final concentration of 1×10^8 colony-forming units (CFU)/ml. In each test, 10 μl of the bacteria suspension was spread

over each sample, which were then covered with another film and gently pressed to spread the inoculums over the entire surface. The inoculated films were incubated at 37°C for 1 hour. Then, 2 ml of PBS was added to wash out survived microbes and bacteria suspensions were plated for CFU counts. This test was repeated with triplicate samples, and blank dish was used as control group. The in vivo evaluation was performed by laminating five different skin patches (1 cm × 1 cm) on healthy human chest for 5 days. The bacterial amounts on the skin patches and skin covered with these patches were examined. In brief, dampened sterile cotton swabs were used to collect the bacteria on the skin where the patch was covered, which were subjected to same cultivation and counting procedures. The bare skin area closely neighboring to samples was evaluated as control group.

Antiviral efficacy test against SARS-CoV-2

Assessment of the antiviral properties was conducted by challenging a 1 × 1 in square coupons of the porous EGaIn composite with and without ε-PL, each in triplicate ($N = 3$). We also included a 1 × 1 in steel coupon as a comparison material. A 10-μl droplet of SARS-CoV-2 at a titer of 3.41×10^7 $TCID_{50}$/ml was pipetted onto each of the coupons followed by a 30-min incubation at room temperature. Ten microliters of the SARS-CoV-2 stock virus was also directly added into 10 ml of DMEM [supplemented with 10% FBS and (2×) antimycotic-antibiotic] as a positive control. After incubation, each coupon was collected into a 50-ml conical tube containing 10 ml of DMEM [supplemented with 10% FBS and (2×) antimycotic-antibiotic]. The tubes were inverted 5 to 10 times and then briefly vortexed for 10 s. A $TCID_{50}$ assay was then conducted using three 96-well plates that were seeded the previous day with 20,000 Vero E6 cells per well and a volume of 200 μl of medium per well. DMEM (200 μl) [supplemented with 10% FBS and (2×) antimycotic-antibiotic] in each well was carefully removed, which was then filled with 222 μl of the as-prepared solutions from the conical tubes. The resulting solution (22 μl) was then serially diluted by 5 to 10 times. Once the final serial dilution has been completed, the extra remaining 22 μl was discarded in the appropriate disinfectant. This process was repeated for the three samples of the porous composite without ε-PL on plate 2 and the steel coupon on plate 3. The three plates were placed in the 37°C (5% CO_2) incubator for 72 hours. The plates were then analyzed for the presence of the cytopathic effect (CPE) in each of the wells. The results of CPE presence were then used to calculate the $TCID_{50}$/ml titer using the improved Kärber method/Sun method (*51*).

Experiments on human subjects

The on-body evaluations of skin-interfaced devices on human participants were conducted under approval from Institutional Review Board at the University of Missouri-Columbia (number 2010272). All human subjects gave written and informed consent before participation in the studies.

Statistical analysis

The statistical analysis was performed using GraphPad Prism 8.0 software. Differences among groups were evaluated using one-way analysis of variance (ANOVA) followed by Tukey's multiple comparisons test. The values of $P < 0.05$ were considered statistically significant.

Supplementary Materials

This PDF file includes:
Figs. S1 to S35
Table S1
References

Other Supplementary Material for this manuscript includes the following:
Movies S1 and S2

REFERENCES AND NOTES

1. J. A. Rogers, T. Someya, Y. Huang, Materials and mechanics for stretchable electronics. *Science* **327**, 1603–1607 (2010).
2. D. H. Kim, N. Lu, R. Ma, Y. S. Kim, R. H. Kim, S. Wang, J. Wu, S. M. Won, H. Tao, A. Islam, K. J. Yu, T. I. Kim, R. Chowdhury, M. Ying, L. Xu, M. Li, H. J. Chung, H. Keum, M. McCormick, P. Liu, Y. W. Zhang, F. G. Omenetto, Y. Huang, T. Coleman, J. A. Rogers, Epidermal electronics. *Science* **333**, 838–843 (2011).
3. D. C. Kim, H. J. Shim, W. Lee, J. H. Koo, D. H. Kim, Material-based approaches for the fabrication of stretchable electronics. *Adv. Mater.* **32**, 1902743 (2020).
4. K. Sim, Z. Rao, F. Ershad, C. Yu, Rubbery electronics fully made of stretchable elastomeric electronic materials. *Adv. Mater.* **32**, 1902417 (2020).
5. T. C. Shyu, P. F. Damasceno, P. M. Dodd, A. Lamoureux, L. Xu, M. Shlian, M. Shtein, S. C. Glotzer, N. A. Kotov, A kirigami approach to engineering elasticity in nanocomposites through patterned defects. *Nat. Mater.* **14**, 785–789 (2015).
6. T. Someya, Z. Bao, G. G. Malliaras, The rise of plastic bioelectronics. *Nature* **540**, 379–385 (2016).
7. Y. Ohm, C. Pan, M. J. Ford, X. Huang, J. Liao, C. Majidi, An electrically conductive silver–polyacrylamide–alginate hydrogel composite for soft electronics. *Nat. Electron.* **4**, 185–192 (2021).
8. K. Sakuma, *Flexible, Wearable, and Stretchable Electronics* (CRC Press, 2020).
9. S. Choi, S. I. Han, D. Jung, H. J. Hwang, C. Lim, S. Bae, O. K. Park, C. M. Tschabrunn, M. Lee, S. Y. Bae, J. W. Yu, J. H. Ryu, S. W. Lee, K. Park, P. M. Kang, W. B. Lee, R. Nezafat, T. Hyeon, D. H. Kim, Highly conductive, stretchable and biocompatible Ag-Au core-sheath nanowire composite for wearable and implantable bioelectronics. *Nat. Nanotechnol.* **13**, 1048–1056 (2018).
10. Y. Kim, J. Zhu, B. Yeom, M. di Prima, X. Su, J. G. Kim, S. J. Yoo, C. Uher, N. A. Kotov, Stretchable nanoparticle conductors with self-organized conductive pathways. *Nature* **500**, 59–63 (2013).
11. N. Matsuhisa, D. Inoue, P. Zalar, H. Jin, Y. Matsuba, A. Itoh, T. Yokota, D. Hashizume, T. Someya, Printable elastic conductors by in situ formation of silver nanoparticles from silver flakes. *Nat. Mater.* **16**, 834–840 (2017).
12. S. Chen, H.-Z. Wang, R.-Q. Zhao, W. Rao, J. Liu, Liquid metal composites. *Matter* **2**, 1446–1480 (2020).
13. E. J. Markvicka, M. D. Bartlett, X. Huang, C. Majidi, An autonomously electrically self-healing liquid metal–elastomer composite for robust soft-matter robotics and electronics. *Nat. Mater.* **17**, 618–624 (2018).
14. Y. Liu, X. Ji, J. Liang, Rupture stress of liquid metal nanoparticles and their applications in stretchable conductors and dielectrics. *npj Flex. Electron.* **5**, 11 (2021).
15. L. Zheng, M. Zhu, B. Wu, Z. Li, S. Sun, P. Wu, Conductance-stable liquid metal sheath-core microfibers for stretchy smart fabrics and self-powered sensing. *Sci. Adv.* **7**, eabg4041 (2021).
16. Z. Ma, Q. Huang, Q. Xu, Q. Zhuang, X. Zhao, Y. Yang, H. Qiu, Z. Yang, C. Wang, Y. Chai, Z. Zheng, Permeable superelastic liquid-metal fibre mat enables biocompatible and monolithic stretchable electronics. *Nat. Mater.* **20**, 859–868 (2021).
17. S. Xu, A. Jayaraman, J. A. Rogers, Skin sensors are the future of health care. *Nature* **571**, 319–321 (2019).
18. C. Marambio-Jones, E. Hoek, A review of the antibacterial effects of silver nanomaterials and potential implications for human health and the environment. *J. Nanopart. Res.* **12**, 1531–1551 (2010).
19. A. K. Chatterjee, R. Chakraborty, T. Basu, Mechanism of antibacterial activity of copper nanoparticles. *Nanotechnology* **25**, 135101 (2014).
20. J. J. Kim, S. Ha, L. Kim, Y. Kato, Y. Wang, C. Okutani, H. Wang, C. Wang, K. Fukuda, S. Lee, T. Yokota, O. S. Kwon, T. Someya, Antimicrobial second skin using copper nanomesh. *Proc. Natl. Acad. Sci. U.S.A.* **119**, e2200830119 (2022).
21. R. Ye, H. Xu, C. Wan, S. Peng, L. Wang, H. Xu, Z. P. Aguilar, Y. Xiong, Z. Zeng, H. Wei, Antibacterial activity and mechanism of action of ε-poly-l-lysine. *Biochem. Biophys. Res. Commun.* **439**, 148–153 (2013).

22. Y.-Q. Li, Q. Han, J.-L. Feng, W.-L. Tian, H.-Z. Mo, Antibacterial characteristics and mechanisms of ε-poly-lysine against *Escherichia coli* and *Staphylococcus aureus*. *Food Control* **43**, 22–27 (2014).
23. M. Hosoya, J. Neyts, N. Yamamoto, D. Schols, R. Smoeck, R. Pauwels, E. de Clercq, Inhibitory effects of polycations on the replication of enveloped viruses (HIV, HSV, CMV, RSV, influenza A virus and togaviruses) in vitro. *Antivir. Chem. Chemother.* **2**, 243–248 (1991).
24. N. Langeland, L. J. Moore, H. Holmsen, L. Haarr, Interaction of polylysine with the cellular receptor for herpes simplex virus type 1. *J. Gen. Virol.* **69**, 1137–1145 (1988).
25. B. Binks, S. Lumsdon, Pickering emulsions stabilized by monodisperse latex particles: Effects of particle size. *Langmuir* **17**, 4540–4547 (2001).
26. K. J. Bretz, Á. Jobbagy, K. Bretz, Force measurement of hand and fingers. *Biomech. Hung.* **3**, 61–66 (2010).
27. M. J. Hessert, M. Vyas, J. Leach, K. Hu, L. A. Lipsitz, V. Novak, Foot pressure distribution during walking in young and old adults. *BMC Geriatr.* **5**, 8 (2005).
28. S. Liu, D. S. Shah, R. Kramer-Bottiglio, Highly stretchable multilayer electronic circuits using biphasic gallium-indium. *Nat. Mater.* **20**, 851–858 (2021).
29. M. H. Malakooti, N. Kazem, J. Yan, C. Pan, E. J. Markvicka, K. Matyjaszewski, C. Majidi, Liquid metal supercooling for low-temperature thermoelectric wearables. *Adv. Funct. Mater.* **29**, 1906098 (2019).
30. T. Someya, M. Amagai, Toward a new generation of smart skins. *Nat. Biotechnol.* **37**, 382–388 (2019).
31. S. Chao, Y. Li, R. Zhao, L. Zhang, Y. Li, C. Wang, X. Li, Synthesis and characterization of tigecycline-loaded sericin/poly (vinyl alcohol) composite fibers via electrospinning as antibacterial wound dressings. *J. Drug Deliv. Sci. Technol.* **44**, 440–447 (2018).
32. X. Zheng, H. Lee, T. H. Weisgraber, M. Shusteff, J. DeOtte, E. B. Duoss, J. D. Kuntz, M. M. Biener, Q. Ge, J. A. Jackson, S. O. Kucheyev, N. X. Fang, C. M. Spadaccini, Ultralight, ultrastiff mechanical metamaterials. *Science* **344**, 1373–1377 (2014).
33. S. Liu, Y. Rao, H. Jang, P. Tan, N. Lu, Strategies for body-conformable electronics. *Matter* **5**, 1104–1136 (2022).
34. L. Tian, B. Zimmerman, A. Akhtar, K. J. Yu, M. Moore, J. Wu, R. J. Larsen, J. W. Lee, J. Li, Y. Liu, B. Metzger, S. Qu, X. Guo, K. E. Mathewson, J. A. Fan, J. Cornman, M. Fatina, Z. Xie, Y. Ma, J. Zhang, Y. Zhang, F. Dolcos, M. Fabiani, G. Gratton, T. Bretl, L. J. Hargrove, P. V. Braun, Y. Huang, J. A. Rogers, Large-area MRI-compatible epidermal electronic interfaces for prosthetic control and cognitive monitoring. *Nat. Biomed. Eng.* **3**, 194–205 (2019).
35. N. Driscoll, B. Erickson, B. B. Murphy, A. G. Richardson, G. Robbins, N. V. Apollo, G. Mentzelopoulos, T. Mathis, K. Hantanasirisakul, P. Bagga, S. E. Gullbrand, M. Sergison, R. Reddy, J. A. Wolf, H. I. Chen, T. H. Lucas, T. R. Dillingham, K. A. Davis, Y. Gogotsi, J. D. Medaglia, F. Vitale, MXene-infused bioelectronic interfaces for multiscale electrophysiology and stimulation. *Sci. Transl. Med.* **13**, eabf8629 (2021).
36. J. F. Schenck, The role of magnetic susceptibility in magnetic resonance imaging: MRI magnetic compatibility of the first and second kinds. *Med. Phys.* **23**, 815–850 (1996).
37. A. L. Byrd, Y. Belkaid, J. A. Segre, The human skin microbiome. *Nat. Rev. Microbiol.* **16**, 143–155 (2018).
38. Y. Su, Z. Zhi, Q. Gao, M. Xie, M. Yu, B. Lei, P. Li, P. X. Ma, Autoclaving-derived surface coating with in vitro and in vivo antimicrobial and antibiofilm efficacies. *Adv. Healthc. Mater.* **6**, 1601173 (2017).
39. J.-H. Kim, S. Kim, J.-H. So, K. Kim, H.-J. Koo, Cytotoxicity of gallium–indium liquid metal in an aqueous environment. *ACS Appl. Mater. Interfaces* **10**, 17448–17454 (2018).
40. A. J. Bandodkar, V. W. S. Hung, W. Jia, G. Valdés-Ramírez, J. R. Windmiller, A. G. Martinez, J. Ramírez, G. Chan, K. Kerman, J. Wang, Tattoo-based potentiometric ion-selective sensors for epidermal pH monitoring. *Analyst* **138**, 123–128 (2013).
41. H. U. Chung, B. H. Kim, J. Y. Lee, J. Lee, Z. Xie, E. M. Ibler, K. H. Lee, A. Banks, J. Y. Jeong, J. Kim, C. Ogle, D. Grande, Y. Yu, H. Jang, P. Assem, D. Ryu, J. W. Kwak, M. Namkoong, J. B. Park, Y. Lee, D. H. Kim, A. Ryu, J. Jeong, K. You, B. Ji, Z. Liu, Q. Huo, X. Feng, Y. Deng, Y. Xu, K. I. Jang, J. Kim, Y. Zhang, R. Ghaffari, C. M. Rand, M. Schau, A. Hamvas, D. E. Weese-Mayer, Y. Huang, S. M. Lee, C. H. Lee, N. R. Shanbhag, A. S. Paller, S. Xu, J. A. Rogers, Binodal, wireless epidermal electronic systems with in-sensor analytics for neonatal intensive care. *Science* **363**, eaau0780 (2019).
42. Y. Yu, J. Nassar, C. Xu, J. Min, Y. Yang, A. Dai, R. Doshi, A. Huang, Y. Song, R. Gehlhar, A. D. Ames, W. Gao, Biofuel-powered soft electronic skin with multiplexed and wireless sensing for human-machine interfaces. *Sci. Robot.* **5**, eaaz7946 (2020).
43. M. P. Turakhia, D. D. Hoang, P. Zimetbaum, J. D. Miller, V. F. Froelicher, U. N. Kumar, X. Xu, F. Yang, P. A. Heidenreich, Diagnostic utility of a novel leadless arrhythmia monitoring device. *Am. J. Cardiol.* **112**, 520–524 (2013).
44. Z. I. Attia, S. Kapa, F. Lopez-Jimenez, P. M. McKie, D. J. Ladewig, G. Satam, P. A. Pellikka, M. Enriquez-Sarano, P. A. Noseworthy, T. M. Munger, S. J. Asirvatham, C. G. Scott, R. E. Carter, P. A. Friedman, Screening for cardiac contractile dysfunction using an artificial intelligence–enabled electrocardiogram. *Nat. Med.* **25**, 70–74 (2019).
45. S. Mansouri, T. Alhadidi, S. Chabchoub, R. B. Salah, Impedance cardiography: Recent applications and developments. *Biomed. Res.* **29**, 3542–3552 (2018).
46. D. Naranjo-Hernández, J. Reina-Tosina, M. Min, Fundamentals, recent advances, and future challenges in bioimpedance devices for healthcare applications. *J. Sens.* **2019**, 9210258 (2019).
47. Y. Xie, R. Song, D. Yang, H. Yu, C. Sun, Q. Xie, R. X. Xu, Motion robust ICG measurements using a two-step spectrum denoising method. *Physiol. Meas.* **42**, 095004 (2021).
48. K. Ushimaru, Y. Hamano, H. Katano, Antimicrobial activity of ε-poly-L-lysine after forming a water-insoluble complex with an anionic surfactant. *Biomacromolecules* **18**, 1387–1392 (2017).
49. H.-W. Zhu, H. L. Gao, H. Y. Zhao, J. Ge, B. C. Hu, J. Huang, S. H. Yu, Printable elastic silver nanowire-based conductor for washable electronic textiles. *Nano Res.* **13**, 2879–2884 (2020).
50. P. Li, Y. F. Poon, W. Li, H. Y. Zhu, S. H. Yeap, Y. Cao, X. Qi, C. Zhou, M. Lamrani, R. W. Beuerman, E. T. Kang, Y. Mu, C. M. Li, M. W. Chang, S. S. Jan Leong, M. B. Chan-Park, A polycationic antimicrobial and biocompatible hydrogel with microbe membrane suctioning ability. *Nat. Mater.* **10**, 149–156 (2011).
51. C. Lei, J. Yang, J. Hu, X. Sun, On the calculation of $TCID_{50}$ for quantitation of virus infectivity. *Virol. Sin.* **36**, 141–144 (2021).
52. Y. Khan, M. L. Mauriello, P. Nowruzi, A. Motani, G. Hon, N. Vitale, J. Li, J. Kim, A. Foudeh, D. Duvio, E. Shols, M. Chesnut, J. Landay, J. Liphardt, L. Williams, K. D. Sudheimer, B. Murmann, Z. Bao, P. E. Paredes, Design considerations of a wearable electronic-skin for mental health and wellness: Balancing biosignals and human factors. bioRxiv 2021.01.20.427496 [Preprint]. 21 January 2021. https://doi.org/10.1101/2021.01.20.427496.
53. N. Cohen, K. Bhattacharya, A numerical study of the electromechanical response of liquid metal embedded elastomers. *Int. J. Non-Linear Mech.* **108**, 81–86 (2019).
54. M. Geerligs, L. van Breemen, G. Peters, P. Ackermans, F. Baaijens, C. Oomens, In vitro indentation to determine the mechanical properties of epidermis. *J. Biomech.* **44**, 1176–1181 (2011).
55. M. L. Crichton, B. C. Donose, X. Chen, A. P. Raphael, H. Huang, M. A. F. Kendall, The viscoelastic, hyperelastic and scale dependent behaviour of freshly excised individual skin layers. *Biomaterials* **32**, 4670–4681 (2011).

Acknowledgments

Funding: Z.Y. acknowledges the financial support from the start-up fund of the University of Missouri-Columbia. J.X. acknowledges the financial support from the start-up fund of the University of Nebraska Medical Center and National Institute of General Medical Sciences (NIGMS) and National Institute of Arthritis and Musculoskeletal and Skin Diseases (NIAMS) of National Institutes of Health (award numbers: P30GM127200 and R21AR080906). G.H. acknowledge the Air Force Office of Scientific Research, USA under grant no. AF 9550-20-1-0279 with program manager B. (Les) Lee and the Office of Naval Research, USA under grant no. FA9550-21-1-0226 with program manager A. Rahman. C.K. and Q.C. acknowledge support from Air Force Office of Scientific Research grant AFOSR FA9550-20-1-0257. S.M. acknowledges the financial support from the National Science Foundation (award number: 2149721). **Author contributions:** Z.Y., Y.X., and J.X. conceived the idea and led research efforts. Y.X., Y.S., X.X., B.A., G.Z., D.N.A., H.H., S.P.R., J.L.S., C.K., Z.C., S.M., Y.L., A.B., Q.C., G.H., J.X., and Z.Y. performed experiments and data analysis. Y.S. and J.X. performed antibacterial and cytotoxicity tests. D.N.A., S.P.R., and J.L.S. performed antiviral tests. X.X. and G.H. conducted the numerical simulations. Z.Y., Y.X., and J.X. wrote the manuscript with assistance of other coauthors. **Competing interests:** The authors declare that they have no competing interests. **Data and materials availability:** All data needed to evaluate the conclusions in the paper are present in the paper and/or the Supplementary Materials.

Submitted 26 September 2022
Accepted 2 December 2022
Published 6 January 2023
10.1126/sciadv.adf0575